

31 **Abstract**

32 Rohrschollen Island is an artificial island of the large Upper Rhine River whose
33 geometry and hydrological dynamics are the result of engineering works during the 19th and
34 20th centuries. Before its channelization, the Rhine River was characterized by an intense
35 hydro-morphological activity which maintained a high level of biodiversity along the fluvial
36 corridor. This functionality considerably decreased during the two last centuries. Since 2012,
37 a restoration project was launched to reactivate typical alluvial processes, including bedload
38 transport, lateral channel dynamics and surface-subsurface water exchanges. An integrated
39 hydrological model has been applied to the area of Rohrschollen Island to assess the
40 efficiency of the restoration regarding surface and subsurface flows. This model is calibrated
41 using measured piezometric heads. Simulated patterns of water exchanges between the
42 surface and subsurface compartments of the Island are checked against the information
43 derived from thermal infrared imaging. The simulated results are then used to better
44 understand the evolutions of the infiltration/exfiltration zones over time and space and to
45 determine the physical controls of surface-subsurface interactions on the hydrographic
46 network of Rohrschollen Island. The use of integrated hydrological modeling has proven to be
47 an efficient approach to assess the efficiency of restoration actions regarding surface and
48 subsurface flows.

49

50 **Keywords**

51 Surface-subsurface water interactions, Integrated hydrological modeling, flood restoration,
52 Thermal infrared imagery, Rohrschollen Island, Upper Rhine River.

53

54 **Highlights** (less than 85 characters, including spaces)

55 - Direct hydrological impacts of restoration on a riverine island are modeled.

- 56 - Integrated modeling captures the hydrologic surface-subsurface interactions.
- 57 - Simulated exfiltration areas are also located by thermal infrared imaging.
- 58 - Management practices can be optimized on the basis of simulated system responses.

59

60 **1. Introduction**

61 Interactions between surface and subsurface flow processes are key components of the
62 continental hydrological cycle (Winter, 1995; Sophocleous, 2002), which have received
63 particular attention in the last decades partly because of their substantial impact on the overall
64 response of hydrologic systems (Boano et al., 2014; Brunner et al., 2017, and citations
65 herein). Several studies have recently highlighted the hydrological interactions between
66 surface and subsurface that have a major impact on the biogeochemical and ecological
67 responses of hydrosystems (e.g., Stegen et al., 2016; Danczak et al., 2016; Partington et al.,
68 2017; Stegen et al., 2018). These interactions, which are partly driven by the
69 geomorphological structure and the channel dynamics (Namour et al., 2015), influence flow
70 pathways, water mixing, residence time in the hyporheic zone along streambeds, and the
71 overall ecological functioning (Schmitt et al., 2011). They are complex for several reasons,
72 including (a) the nonlinearity of the processes involved, (b) the strong heterogeneity of the
73 hydrological systems, and (c) the incidence of small-scale features on large-scale behavior
74 (Hester et al., 2017). Although these surface-subsurface interactions have been extensively
75 investigated in the last decades, several issues relating to them require a deeper understanding
76 to address contemporary challenges associated with water quality and water resources
77 management (Brunner et al., 2017). Among these issues, monitoring and modeling the
78 evolution of these interactions over space and time is fundamental (Krause et al., 2014),
79 especially in the context of river restoration.

80 River restoration has been applied worldwide to counteract the undesired effects of
81 anthropogenic actions on river ecosystems and ecosystem services (e.g., Wohl et al., 2015,
82 and citations herein). From a general perspective, the goal of restoration projects is to enhance
83 the hydrological, biogeochemical, and ecological functioning of large rivers and stream
84 hydrosystems through the reactivation of lost geophysical, geochemical, or biological
85 processes. Due to their firm control on biogeochemical and ecological signatures in the so-
86 called hyporheic zone (e.g., Peralta-Maraver et al., 2018), the interactions between surface
87 and subsurface hydrological processes may become a focus of restoration projects (e.g.,
88 Boulton et al., 2010; Friberg et al., 2017). As examples, surface-subsurface water exchanges
89 generate oxygen/carbon transfers (e.g., Stegen et al., 2016; Danczak et al., 2016) and thermal
90 refuges for various aquatic species (e.g., Kurylyk et al., 2015), they also revive ponding and
91 renewal of water in wetlands that could otherwise turn to perishing swamps partly
92 disconnected from stream flow. Many projects try to improve the water quality and/or
93 ecological processes of the hydrosystem through engineering works that target hyporheic
94 exchange enhancements. Maintaining or amplifying these interactions could reveal crucial
95 regarding climate change effects to preserve aquatic species. Nevertheless, it is still very
96 difficult to assess the efficiency of such restoration projects as this requires a refined
97 characterization of the location and amplitude of surface-subsurface interactions (e.g.,
98 Morandi et al., 2014).

99 Several advances in measurement techniques and modeling approaches appear very
100 promising to improve our current understanding and our forecasting capabilities regarding
101 surface-subsurface interactions (Krause et al., 2014; Brunner et al., 2017). Many
102 experimental/field projects are related to the use of temperature as a tracer of hydrological
103 connectivity and locations where groundwater discharges into surface water bodies (e.g.,
104 Pfister et al., 2010; Daniluk et al., 2013). Two different thermal techniques—Fiber Optic-

105 Distributed Temperature Sensing (FO-DTS) and Thermal InfraRed (TIR) survey—have been
106 used for their potential to inform on spatial and temporal patterns of water fluxes in large
107 areas of the hyporheic zone through the determination of thermal anomalies. FO-TDS
108 provides one-dimensional profiles of these anomalies with a fine spatial resolution by
109 submerging fiber optic cables along a streambed. TIR survey can be performed from air and
110 satellite, and informs on surface temperature with two-dimensional images of various
111 resolutions (e.g., Hare et al., 2015).

112 For their part, integrated hydrologic models emerged in the late 1990s, and they are
113 now recognized as suitable tools to investigate streamflow generation processes at the
114 catchment scale (e.g., Paniconi and Putti, 2015; Fatichi et al., 2016). Although most integrated
115 models rely on the solution to the 3-D Richards equation to describe subsurface flow (e.g.,
116 Maxwell et al., 2014), alternative low-dimensional approaches that simplify the description of
117 the subsurface compartment (still with some physical meaning) have recently appeared (e.g.,
118 Hazenberg et al., 2015, 2016; Jeannot et al., 2018). Solving the 3-D Richards equation with a
119 proper discretization to capture the complex and small-scale physics of flow in the vadose
120 zone over large areas may require substantial computational resources. Low-dimensional
121 integrated approaches that are efficient regarding computation time could also reveal
122 beneficial to tackle practical water management issues. Integrated models, irrespective of their
123 level of complexity, explicitly account for the interaction between surface and subsurface
124 hydrological processes. Thus, their application to hydrosystems renders insights on the
125 evolution over time and space of surface-subsurface interactions (e.g., Partington et al., 2013;
126 Camporese et al., 2014).

127 Hydrologic modeling has already been used to assess the potential effects of
128 restoration works on the hydrologic response of a given system. The studies reported in the
129 ongoing literature are mainly geared towards the effect of restoration on subsurface water

130 table dynamics (e.g., Ohara et al., 2014), floodplain responses (e.g., Martinez et al., 2014;
131 Clilverd et al., 2016), and vegetation dynamics (e.g., Hammersmark et al., 2010). To our
132 knowledge, the prediction with models of hyporheic exchanges has not yet been considered.
133 No integrated hydrologic model has been applied to a restored fluvial hydrosystem even
134 though the application could reveal noteworthy data in rendering quantitative indicators of
135 restoration efficiency. In addition, the combined use of thermal information with integrated
136 hydrological models is not yet common even though comparing and discussing both seems
137 fruitful. Ala-aho et al. (2015) used thermal imaging and integrated modeling to study the
138 exchanges between groundwater and lakes in Finland. Glaser et al. (2016) used integrated
139 modeling and TIR survey to improve the calibration procedure and investigate the dynamics
140 of the saturated area in a small catchment in Luxembourg. Munz et al. (2017) combined
141 thermal measurement along the banks of a stream and integrated modeling at the reach scale
142 to improve the determination of residence times in the hyporheic zone.

143 In this paper, a low-dimensional integrated hydrologic model NIHM (for Normally
144 Integrated Hydrologic Model) is applied to the restored hydrosystem of Rohrschollen Island ,
145 which is an artificial island located 8 km south of Strasbourg (Upper Rhine, France, see Fig.
146 1-a). Previous studies have shown that the hydrological, sedimentological and
147 geomorphological dynamics of the Island were very active due to intense hyporheic
148 exchanges and surface processes (Eschbach et al., 2017; 2018). These dynamics were tightly
149 linked to the flood dynamics of the Rhine River that were progressively lost because of
150 territorial developments along the Rhine fluvial corridor. A restoration project started in 2012
151 with the idea of improving the overall functioning of the ecosystem through artificial
152 injections. The restoration actions specifically target short-term enhancement of hyporheic
153 exchanges over the whole Island and the reactivation of sediment transport in the main
154 channel of the Island. Even though short-term horizon effects are the main target of the

155 restoration, it is expected that duplicating over time flooding episodes in the Island could
156 result in beneficial impacts on long-term ecological and biological health of the Island.

157 The proposed study addresses and models a couple of these flooding episodes with the
158 four main objectives that are : (i) to test the performance of NIHM regarding the description
159 of highly transient hydrologic behavior over short periods of time; (ii) to check on the
160 correspondences and discrepancies between model results and TIR imaging in the delineation
161 of exfiltration patterns; (iii) to investigate on the efficiency of restoration actions undertaken
162 at Rohrschollen Island, especially regarding surface-subsurface water exchanges, and (iv) to
163 propose optimal short-term management procedures regarding the enhancement of surface-
164 subsurface exchanges.

165 It could be argued that short-term analysis of a restored system does not fit the general
166 understanding stating that restoration processes are intended to render benefits over long-term
167 horizons. In the present case (but also in many other cases), restoration works are recent and
168 the system is still evolving. This means that long-term simulations on the basis of the actual
169 settings of the system would probably miss its further evolution. It makes sense to assess the
170 behavior of a recently restored hydrosystem in response to short-terms events. Duplicating
171 calculations for various short "stress" periods, is also a way to foresee how the system could
172 behave, even though uncertainty and model robustness associated with the evolution of the
173 system over time persist. This study is limited to the analysis of the short-term response (to
174 flood events that are also pulse stresses) of a transient hydrosystem via a highly resolved
175 model in time and space.

176

177 **2. Data and hydrological modeling**

178 *2.1. Study Area – Rohrschollen Island*

179 *2.1.1 General description*

180 Rohrschollen Island is the result of historical engineering works carried out along the
181 Rhine River mainly to prevent flooding and to develop navigation and agriculture. The
182 hydrological and geomorphological dynamics of the area were massively impacted (Eschbach
183 et al., 2017; Eschbach et al., 2018). Three structures completely control the current geometry
184 and hydraulic behavior of Rohrschollen Island (Fig. 1): (a) the diversion dam (built in 1970)
185 at the southern end of the island that diverts most of the river flow into the Rhine Canal at the
186 western bank of the island, (b) the hydropower plant (built in 1970) located on the Rhine
187 Canal downstream to Rohrschollen Island, and (3) an agricultural dam (built in 1984) at the
188 northern part of the Island to keep a constant water level in the by-passed Old Rhine at the
189 eastern bank of Rohrschollen Island.

190 Rohrschollen Island was regularly flooded in the past (Eschbach et al., 2018). The
191 main anastomosed channel inside the Island, the Bauerngrundwasser (BGW; Fig. 1), was
192 disconnected on its upstream mouth from the Rhine River by the excavation of the Rhine
193 canal. This disconnection, combined with dampened groundwater dynamics along the Island,
194 impacted the hydrological, geomorphological, and ecological functioning of the hydrosystem
195 (Eschbach et al., 2017). The former flood dynamics induced large water table fluctuations,
196 lively interactions between the surface and subsurface domains, intense rejuvenation of
197 habitat mosaic driven by geomorphological processes, and a high level of biodiversity for
198 species of aquatic and riverine habitats. As a result of engineering works performed to control
199 the Rhine River, the ecological services associated with the flood dynamics and the
200 hydrologic connection between the floodplain of the Island and the river were lost.

201 In 2012, the European Union funded a restoration project (LIFE + program) in order to
202 counteract the loss of various natural processes and thus re-establish part of the former
203 dynamics of the system. The Rhine River water is now injected through a floodgate into a 900
204 m long new artificial channel (south to the Island; Fig. 1-b) following rules that relate the

205 injected discharge with the discharge of the Rhine River. A constant discharge of $2 \text{ m}^3\text{s}^{-1}$ –
206 later referred to as the base flow injection – is injected when the discharge of the Rhine River
207 does not exceed $1550 \text{ m}^3\text{s}^{-1}$. When the discharge of the Rhine River rises above this value, the
208 injected discharge is increased accordingly up to a maximum rate of $80 \text{ m}^3 \text{ s}^{-1}$. These
209 injections should contribute to (a) enhancing discharge into the surface water bodies of the
210 Island (especially in the BGW) and partly recovering floods on the Island (floods occur when
211 the injected rate exceeds the top-edge discharge of the new channel at $20 \text{ m}^3\text{s}^{-1}$), (b)
212 recovering bedload transport and lateral channel dynamics (especially along the new channel),
213 (c) activating surface-subsurface interactions, and (d) stimulating the renewal of aquatic and
214 riverine ecosystems. Overall, it is worth noting that the hydrologic behavior of Rohrschollen
215 Island is primarily controlled by water levels in the Old Rhine and the Rhine Canal (regulated
216 by the two dams and the hydropower plant mentioned above), and by the injection discharge
217 in the new channel.

218 *2.1.2 Hydrologic monitoring*

219 A large interdisciplinary environmental monitoring was conducted to investigate the
220 effects and the efficiency of the restoration, but also to check on some risks such as the
221 eventual collapsing of the new channel banks under strong water injections. As an example, a
222 dense network of piezometers (yellow squares in Fig. 1-c) was installed along both the
223 artificial new channel and the BGW. More precisely, ten transects along these channels were
224 instrumented with a piezometer on each channel bank. The time resolution of measurements
225 in the 20 piezometers ranges from 5 min along the new channel to 10 min along the BGW.
226 This network is particularly crucial for hydrological model calibration and to understand the
227 interactions between groundwater and surface water bodies. Other subsurface head
228 measurements are also available on the eastern and western sides of the island. The French
229 National Electricity Company (EDF) is operating devices at the western side of the Island

230 (along the Rhine Canal) to monitor the state of the dike road (blue squares in Fig. 1-c) and, as
231 the owner and manager of the Rohrschollen Island Nature Reserve, the city of Strasbourg is
232 following subsurface water table dynamics at the eastern side (orange squares in Fig. 1-c).

233

234 *2.1.3 Historical and sedimentological surveys*

235 Geo-historical and sedimentological surveys were used to reconstruct the morpho-
236 sedimentary temporal trajectory of the Island since the middle of the 18th century. The geo-
237 historical survey is partly based on six old maps, two sets of aerial photographs, and the actual
238 digital elevation model of the Island (see Fig. 2, left part). Planimetric data were
239 georeferenced in a GIS (geographic information system) and processed to highlight the
240 temporal dynamics of the main morpho-ecological units. The sedimentological study was
241 based on seven coring transects distributed along the BGW. Grain size analysis was also
242 performed on sediment samples from three transects and two pits in the floodplain to
243 determine the transport and deposition processes of fine sediments. The combination of the
244 geo-historical and sedimentological analysis helped to reconstruct the sedimentary deposition
245 trajectory and to locate precisely historical gravel bars (see Fig. 2, right side). This
246 information was used to spatialize the parameters of the hydrological model and to preset the
247 initial values of key parameters related to the composition of the sediment units. More details
248 on this part of the study can be found in Eschbach et al. (2018).

249

250 *2.1.4. Thermal infrared imaging*

251 Thermal infrared imaging (TIR) was carried out at Rohrschollen Island to investigate
252 the relationship between the evolution of some geomorphological features (e.g., riffles and
253 pools) and the interactions between surface and subsurface waters. A FLIR b425 infrared
254 camera was fixed under a paraglider to take pictures covering the whole island. The camera

255 was calibrated using several key parameters such as water emissivity and the height above the
 256 topography. The flight took place on January 22, 2015, a date chosen to have minimal canopy
 257 extension and maximal temperature contrast between surface and subsurface waters (with
 258 approximately 4°C surface temperature and 10°C groundwater temperature). The thermal
 259 images were processed to locate thermal anomalies along the new artificial channel and the
 260 BGW. The radiance was first converted into temperature using Planck’s law and in-situ
 261 measurements as references. The temperature maps were then georeferenced, and pixels
 262 associated with high uncertainty on temperatures were also discarded. Further treatments
 263 based on optic images (in the visible wavelengths) delineated and located surface objects such
 264 as banks, vegetation, logjams, and gravel bars. Further details about thermal image processing
 265 can be found in Eschbach et al. (2017).

266 *2.2. Hydrological modeling strategy*

267 *2.2.1. The Normally Integrated Model (NIHM)*

268 The integrated hydrological model used to model Rohrschollen Island is the Normally
 269 Integrated Hydrologic Model (NIHM) (Pan et al., 2015; Weill et al., 2017; Jeannot et al.,
 270 2018). This tool is a physically based and spatially fully-distributed model that describes flow
 271 processes in the surface and subsurface domains of a catchment and their couplings. For the
 272 sake of simplicity, only the model parts used for this study are presented here. A detailed
 273 presentation of the model (primarily concerning treatment of the flow equations) is available,
 274 for example, in Jeannot et al. (2018).

275 The subsurface flow processes are described using a low-dimensional equation that
 276 results from the integration of the 3-D Richards equation along a direction normal to the
 277 bedrock (i.e., the impervious bottom of the aquifer). The final equation for subsurface flow
 278 can be written as:

$$279 \quad \frac{\partial \bar{\theta}}{\partial t} + \bar{S}(h) \frac{\partial h}{\partial t} + \nabla_{x,y} \cdot (-\bar{\mathbf{T}} \theta \nabla_{x,y} h) = Q_w \quad [1]$$

280 where $\bar{\theta} h = \int_{z_w}^{z_s} \theta z dz$, $\bar{S} h = S_{sat} h$, $\bar{\mathbf{T}}(h, \theta) = \mathbf{K}_{sat} h + \int_{z_w}^{z_s} \mathbf{K} \theta z dz$. \mathbf{K}_{sat} , and S_{sat} are
281 averages along the integration direction z of the saturated hydraulic conductivity tensor and
282 the specific storage capacity in the saturated zone, respectively. θ [-] is the water content; \mathbf{K}
283 [LT^{-1}] is the tensor of hydraulic conductivity; h [L] is the hydraulic head (or the capillary
284 head); and Q_w [LT^{-1}] is a source term that accounts for the subsurface interactions with both
285 the 1-D river network and the 2-D overland flow. It is worth noting that the 1-D river network
286 compartment was not used in this study because the precision of the digital elevation model
287 (Fig. 2, left) was enough to delineate and model streams, channels, and other small water
288 routing in slight topographic depressions of the 2-D overland flow layer.

289 The 2-D overland flow layer is described using the so-called diffusive wave equation,
290 which is written as:

$$291 \quad \frac{\partial h_s + z_s}{\partial t} - \nabla_x \cdot T_{s,x} \nabla_x h_s + z_s - \nabla_y \cdot T_{s,y} \nabla_y h_s + z_s = q \quad [2]$$

292 with

$$T_{s,x} = \frac{h_s^{5/3}}{N_{man,x}^2 \beta \nabla h_s + z_s} \quad ; \quad T_{s,y} = \frac{h_s^{5/3}}{N_{man,y}^2 \beta \nabla h_s + z_s}$$

293

$$\beta \nabla h_s + z_s = \left[\left(\frac{\partial h_s + z_s}{\partial x} \right)^2 \frac{1}{N_{man,x}^4} + \left(\frac{\partial h_s + z_s}{\partial y} \right)^2 \frac{1}{N_{man,y}^4} \right]^{1/4}$$

294 h_s [L] is the water depth at the surface; z_s [L] is the soil surface elevation; u_x and u_y [LT^{-1}]
295 are the water velocity components along the x and y directions (that are locally defined in the
296 plane normal to the direction of integration z of Eq. (1)); q [LT^{-1}] is a source term including
297 the exchanges with the 1-D river flow compartment and with the subsurface; and $N_{man,x}$ and
298 $N_{man,y}$ [$\text{L}^{-1/3}\text{T}$] are the Manning coefficients in the x and y directions, respectively.

299 The coupling between Eq. (1) and Eq. (2) relies upon a first order law stating that the
 300 flux exchanged between surface and subsurface flows is proportional to the head gradient
 301 between the two compartments. The exchanged flux $Q_{Ex,2D\leftrightarrow SS}$ [LT⁻¹] can be formalized as:

$$302 \quad Q_{Ex,2D\leftrightarrow SS} = K_{Int} \frac{(z_s + h_s) - h}{l_e} F_s \quad [3]$$

$$303 \quad F_s = \min \left[\left(\frac{h_s}{h_{ob}} \right)^{2^{1-h_s/h_{ob}}} ; 1 \right] \quad [4]$$

304 where K_{Int} [LT⁻¹] is the vertical hydraulic conductivity at the interface between the surface
 305 and subsurface compartments; l_e is a user-defined coupling length (i.e., an empirical
 306 thickness of the interface between surface and subsurface compartments); F_s [-] is a scaling
 307 function accounting for the saturated-unsaturated character of the interface between the
 308 surface and subsurface; and h_{ob} is the total obstruction height accounting for small
 309 irregularities of the topography.

310 Regarding the numerical solution, both equations are solved together in a fully implicit
 311 manner using advanced numerical schemes. Note that both equations are two-dimensional and
 312 that only one computation mesh mimicking the topographic surface of the system is required
 313 for simulating both surface and subsurface processes, including their interactions. It is worth
 314 noting that employing a partly simplified model is an incentive to the duplication of
 315 calculations, as is necessary for example when solving inverse problems, evaluating model
 316 sensitivities, and testing hypotheses. This possibility is not exploited in this study which can
 317 be seen as a test of feasibility to capture the short-term very transient dynamics of a
 318 hydrological system via a model highly-resolved in time and space. Simulations discussed
 319 below take between 5 and 24 hours of calculation (for simulation times of 7 to 45 days
 320 respectively) on a single core of a modern processor. Duplicating calculations for the

321 purposes mentioned above remains tractable by distributing the calculation load over multiple
322 cores.

323

324 *2.2.2 Model setup and parametrization*

325 The computation mesh for all the simulations of the study was built from data from an
326 airborne LIDAR survey performed in 2015 that produced high-resolution images of the
327 topography (50 cm in the horizontal plane and 1-2 cm in elevation). The whole Rohrschollen
328 Island is meshed using triangular elements of 20 m on a side. The exception is a 120 m wide
329 corridor surrounding the new channel and the BGW where a refined spatial resolution of 10 m
330 is used. The higher resolution is assumed to better capture the hydrological dynamics and the
331 surface-subsurface interactions along the surface water bodies of the Island.

332 As mentioned previously, the two key drivers of the hydrological response at
333 Rohrschollen Island are (i) the water levels in the Old Rhine and the Rhine Canal, and (ii) the
334 discharge injected in the artificial channel. In base flow conditions, the routine value of $2 \text{ m}^3 \text{ s}^{-1}$
335 ¹ as the injected discharge brings the equivalent of 20 m of annual rainfall over the whole
336 Island. Moreover, the water table in the Island is always fed by the Old Rhine and the Rhine
337 Canal, reducing considerably the potential effect of evapotranspiration on piezometric levels.
338 Provided that the time horizon of the simulations are rather short (less than 50 days), the
339 meteorological forcing – i.e. rainfall and evapotranspiration – are thus considered negligible
340 in the study. Prescribed-head (Dirichlet) boundary conditions are imposed at the western and
341 eastern banks of Rohrschollen Island for the subsurface model, and they have been
342 documented by measurements collected by the EDF and the city of Strasbourg. These
343 boundary conditions may vary over time, depending on the modeled period and availability of
344 data. The northern and southern parts of the Island were considered as no-flow boundaries.
345 The initial conditions were set up by running the model with consistent boundary conditions

346 for the subsurface and the base flow injection rate of $2 \text{ m}^3 \text{ s}^{-1}$ at the new channel inlet until
347 stable hydrological conditions were reached.

348 Several exploratory calculations were performed by varying a single parameter one at
349 the time to obtain some kind of rough sensitivity analysis. A rigorous sensitivity analysis
350 would have required the analytical differentiation of the state variable derivatives with respect
351 to model parameters, which was out of the topic of a study mainly testing whether
352 hydrological modeling would be suited to quantify the effects of restoration works. These
353 exploratory calculations showed us that the model was mainly sensitive to the values of
354 saturated hydraulic conductivity and the exchange coefficient between the surface and
355 subsurface. The calculations also showed us that the other parameters, for example the
356 Manning's coefficient, were less sensitive. Therefore, only the saturated hydraulic
357 conductivity and the exchange coefficient were considered as variable in space while the other
358 parameters were supposed uniform over the whole Island. The initial spatial distribution of
359 the saturated hydraulic conductivity and the exchange coefficient mainly relies upon patterns
360 drawn from the geo-historical and sedimentological surveys of the island (Eschbach et al.,
361 2018). As an example, Fig. 2 maps three historical snapshots of the main geomorphological
362 units (gravel bars). Corridors around the new channel, the BGW, and the network of paleo-
363 channels visible in the floodplain (see the digital elevation model in Fig. 2), were defined and
364 parametrized separately to account for specific deposition histories resulting in specific
365 sediment grain size. Both the saturated hydraulic conductivity and the exchange coefficient
366 were considered as uniform over zones (subareas) of the modeled domain (a block-
367 heterogeneous system), and the initial spatial delineation of these zones was processed via a
368 GIS.

369 Results from particle size laboratory analysis were used to define the initial values of
370 the hydraulic conductivity, the retention curve parameters of the sediments, and the exchange

371 coefficient between the surface and subsurface. Sediment cores were taken along the artificial
372 channel and the BGW at different depths and locations when the piezometric network of the
373 Island was installed. The samples were then analyzed in the lab to determine their textural and
374 particle size characteristics. The Rosetta model (US Salinity Lab, Riverside, CA) was then
375 used to relate textural properties of soils with the model parameters. Regarding Manning's
376 coefficient, the initial values for the artificial channel and the BGW were set following
377 standard tables and field observations.

378 2.2.3. *Model calibration and validation*

379 The integrated model was calibrated and validated using two periods of time for which
380 high-rate injections in the new artificial channel were carried out. The first period (December
381 9, 2014–December 15, 2014) was used as a model calibration exercise which encompassed
382 two peaks of injection with one reaching $80 \text{ m}^3 \text{ s}^{-1}$. The second selected period (May 15,
383 2015–May 21, 2015) was employed as a validation exercise with three injection peaks, two of
384 them exceeding $70 \text{ m}^3 \text{ s}^{-1}$. In both cases, peak injections superimpose onto a continuous base
385 flow fed by the routine injection of $2 \text{ m}^3 \text{ s}^{-1}$ in the inlet channel. Fig. 3 reports the evolution of
386 the injected flow rates over time at the system inlet for both the calibration and validation
387 periods.

388 After a first simulation employing the initial parametrization (defined in Section 2.2.2),
389 all the parameters were manually calibrated to match up simulated head levels in the
390 subsurface with observations. Both the Root Mean Square Error (RMSE) and the Kling-Gupta
391 Efficiency (KGE) associated with observed heads at the 10 transects cross cutting the new
392 channel and the BGW were used as indicators to evaluate the quality of the simulations. Table
393 1 gathers the initial and optimal (i.e., after calibration) parameter values, showing that –
394 except for the saturated hydraulic conductivity, the exchange coefficient and the Van
395 Genuchten parameters of the deeper part of the subsurface – the optimal parameters are very

396 close to the initial ones. During the calibration process, the initial spatial zonation was also
397 modified even if it was tried to preserve the main spatial units initially defined. More
398 precisely, a few additional zones were delineated, mainly along the new channel and the
399 BGW to account for partly clogged zones that showed delayed or smoothed responses of
400 subsurface heads to infiltration. Fig. 4 maps the final set of parameters for the saturated
401 hydraulic conductivity and the exchange coefficient. The sets of calibrated parameters were
402 then used for simulating the validation period to check whether the calculated subsurface head
403 levels match up to the measured values.

404 It is worth noting here that the calibration exercise was performed over a period where
405 the TIR images were not available, which means, in turn, that the calibration only relied upon
406 measured groundwater head levels as a reference. The goal of the calibration was not to match
407 the exfiltration patterns identified through the TIR imaging. When this information became
408 available, the simulation period used for the calibration was extended to reach the date of the
409 airborne flight (January 22, 2015), and the boundary conditions were updated. The exfiltration
410 patterns were then used as verification information to confirm that the model could properly
411 describe the interactions between surface and subsurface and thus be used as a forecasting
412 tool. Forecasts discussed hereinafter cover optimizations of injections in the artificial channel
413 upstream to the Island, which are mainly supposed to maintain active ponding and wetlands
414 (mainly from groundwater outcrops) over long periods.

415

416 **3. Results and discussion**

417 *3.1. Model outputs*

418 Fig. 5 displays the evolution over time of simulated and observed piezometric heads at
419 two locations (transects) in the island. It also plots simulated versus observed heads for all
420 locations and sampling times used during the calibration period. Heads at transects in Fig. 5

421 were selected to show the best and worst match concerning RMSE between simulation and
422 observation. It is worth noting that before injections peaks, the simulated heads are mainly
423 influenced by the Dirichlet-type boundary conditions on the east and west sides of the Island.
424 Few data (one measure each fifteen days) were available to set up these Dirichlet boundary
425 conditions, and the almost constant-over-time simulated heads before peak injections do not
426 fully match up head transients observed along the BGW. That being said, in general the
427 model adequately reproduces the system dynamics, capturing the two peaks of head response
428 associated with the injection patterns at the new channel inlet. The recession part of the
429 response is also captured well with a slight overestimation of the final head value for transect
430 T8 (Fig. 5, upper left panel). The plot of simulated versus observed heads (Fig. 5, right)
431 confirms that the model tends to overestimate the piezometric heads as more points are
432 located above the 1:1 straight line. This feature is associated with one of the founding
433 assumptions of the model regarding the vadose zone, which is integrated with the saturated
434 zone and can be excessively or not sufficiently capacitive, depending on the mean soil
435 moisture (see Weill et al., 2017). The values of the two performance indicators that are the
436 RMSE and the KGE are satisfying, at 17 cm and 0.93, respectively. Regarding the KGE value
437 of all measured versus simulated heads, the Pearson correlation coefficient is 0.97, the bias
438 ratio is 1, and the variance ratio is 1.07.

439 Fig. 6 depicts the same information as Fig. 5 but for the validation period. The
440 agreement between simulated and measured heads remains good with an RMSE of 24 cm and
441 a KGE of 0.75, associated with a Pearson correlation coefficient of 0.94, a bias ratio of 1, and
442 a variance ratio of 1.24. The decrease of the KGE values from calibration to validation steps
443 does not generate bias between observed and simulated head values. Nevertheless, the
444 variance ratio slightly increases showing that errors between observed and simulated heads
445 also increase from calibration to validation. That being said, both exercises show that the

446 NIHM and its calibrated set of parameters render convincing simulations of the highly
447 transient hydrologic behavior of the system.

448

449 *3.2. Interactions between surface and subsurface in Rohrschollen Island*

450 Once calibration and validation were completed, the ability to capture the interactions
451 between surface and subsurface was checked by comparing the modeled exfiltration patterns
452 simulated on January 22, 2015, with the thermal anomalies identified via airborne TIR
453 imaging performed the same day (see Section 2). In Fig. 7, the thermal anomalies are
454 represented as pink spots, and the simulated exfiltration patterns are represented as colored
455 patches ranging from blue to red as a function of the exfiltration rate. Fig. 7 focuses on the
456 area of the Island where a vast majority of the thermal anomalies were identified. The
457 simulated exfiltration patterns usually coincide with the thermal anomalies from the TIR,
458 even though their spatial extension may be wider than thermal anomalies. This feature can be
459 the consequence of multiple factors, such as (a) the substantial sedimentary heterogeneity of
460 the streambed not sufficiently represented in the model, (b) a spatial resolution of the
461 computation mesh not fine enough to capture the very small-scale surface-subsurface
462 interactions, and (c) the measurement uncertainty plaguing the TIR analysis. Keeping these
463 approximations in mind, the hydrologic model correctly locates the surface-subsurface
464 interactions in the Island and provides flux values that are not accessible via TIR survey.

465 Given that a rigorous sensitivity analysis to model parameters was not undertaken, it
466 could be stated that flawed model parameter values are at the origin of mismatches between
467 TIR images and the exfiltration zones modeled by NIHM. Nevertheless, the macroscopic
468 hydraulic diffusion (the ratio of conductivity to specific storage) is correctly fitted as shown
469 by the good match of observed heads both in time and amplitude. The point is that thermal
470 anomalies are visible at a scale on the order of less than 10 m, which is also the scale of local

471 heterogeneity of clay, sand, gravel, and pebble deposits in alluvial systems. A numerical
472 model handling local heterogeneity at that scale should employ a mesh of 1-2 m resolution. In
473 view of the available data, building this model is unfeasible, except by conjecturing the
474 distribution of hydraulic parameters (as can be done for example in stochastic approaches to
475 the inverse problem). **The lack of data suggests that perfect accuracy cannot be expected, and
476 the mismatch between the measurement and model resolutions is the main reason** for
477 discrepancies between TIR and model delineation of exfiltration zones. In addition and under
478 the present modeling constraints, **we suggest that the quality of model results does not relate
479 to the fact that the model accurately represents data over a single scenario, but rather to the
480 fact that it roughly represents data over multiple different scenarios (events). Unfortunately,
481 we only had one single set of TIR imagery at our river reach.**

482 Fig. 8 and Fig. 9 picture the transient interactions between surface and subsurface and
483 tell us why the banana-shaped exfiltration zone reported in Fig. 7 is close to the junction of
484 the new artificial channel and the BGW. Fig. 8 displays maps of the groundwater head, the
485 surface water thickness, and the exfiltration rates over the whole Island at three different times
486 of the calibration period that are $t = 50$ h (i.e., after the first injection peak); $t = 59$ h (i.e., at
487 the second injection peak); and $t = 1072$ h (i.e., the date of the airborne TIR flight). As
488 evidenced by the snapshots of groundwater head and surface water thickness, the water
489 injected upstream to the island, flowing into the BGW, its dead-ends, and the associated
490 floodplain, rapidly infiltrates, producing an important increase in groundwater levels
491 alongside the new artificial channel (and also the BGW), which had been excavated but was
492 still not clogged with fine sediments. When the maximum injection rate is reached ($t = 59$ h),
493 surface ponding occurs on a significant portion of the Island and the groundwater mounding
494 invades all the upstream part of the BGW. Note that the exfiltration rates (Fig. 8, right) are
495 localized in small topographic depressions during the injection period, and the banana-shaped

496 exfiltration pattern (Fig. 7) is still inactive. The latter pattern only appears during the
497 recession period ($t = 1072$ h) when the strong injection rates have stopped. It appears
498 alongside the BGW in the vicinity of the area where the groundwater level previously
499 increased the most. Fig. 9 represents cross-sections along locations *a* and *b* in Fig. 7 for $t = 59$
500 h and $t = 1072$ h, and reports on the subsurface water head, the surface water elevation (set to
501 the topography elevation when surface water thickness is zero), and infiltration-exfiltration
502 rates. It shows that (a) the topography mainly controls the banana-shaped infiltration-
503 exfiltration zone (depressions in Fig. 9), and (b) the temporal dynamics and amplitude of
504 exfiltration are the combined effect of surface water rapidly flowing toward the system outlet
505 (i.e., surface water thickness diminishes), and a slow recession of the groundwater heads after
506 the main peaks of injected flow rates have vanished.

507 Fig. 10 reports on the evolution over time of the total infiltration and exfiltration
508 fluxes calculated over the whole surface area of the Island during the two peaks calibration
509 period. While the injection rate is kept at $2 \text{ m}^3 \text{ s}^{-1}$, both infiltration and exfiltration fluxes are
510 stable with much more infiltration than exfiltration. When the injected flow rate increases, the
511 infiltrated flux follows a slightly delayed evolution over time, which is very similar to the
512 injection hydrograph (with a two peaks shape, see Fig. 3). Meanwhile, as the hydraulic
513 gradient between surface and subsurface changes at some locations, the exfiltration decreases
514 in areas that turn from an exfiltration to an infiltration regime due to excess of surface water
515 associated with injection peaks. Once the injection of water into the new artificial channel
516 stops, the infiltration flux sharply decreases while the exfiltration flux increases. An
517 exfiltration peak can be observed just at the end of the recession period. It is noteworthy that
518 during the recession period, the exfiltration flux is almost constant over time and kept at a
519 value twice that observed before injection (Fig. 10). In the end, forced water injections at the
520 new channel inlet foster water exfiltration from the subsurface that maintains ponds and

521 wetlands on the surface over long periods (say, approximately 15 days for each injection, as
522 simulated by the model but not reported in Fig. 10).

523

524 *3.3. Efficiency of the restoration actions*

525 One of the issues targeted in this study is to assess the efficiency of hydrological
526 restoration projects. The previous results indicate that water injections in the new channel
527 enhance the interactions between surface and subsurface compartments of the Island, noting
528 that it was observed during the excavation that the new channel had been dug in highly
529 conductive sedimentary formations. It may be interesting to check via a modeling approach
530 what causes differences between the current restored circumstances and a pre-restoration
531 situation. As the pre-restored island is not well documented in terms of hydraulic data, we
532 considered a scenario where the pre-restored island is similar to the current situation
533 (including, e.g., geometry and boundary conditions) with the exception that the newly
534 excavated channel connecting Rohrschollen Island's BGW and the Rhine River is absent.
535 Therefore, no forced injection may occur at the southern boundary of the pre-restored island.
536 The hydrological behavior of the pre-restored situation has been simulated and compared with
537 an actual case where the injection rate in the new channel is at the usual year-round
538 configuration of $2 \text{ m}^3\text{s}^{-1}$.

539 Fig. 11 displays snapshots of exfiltration rates in a subarea of the Island for the pre-
540 restored and the restored scenarios. Even with an injected flow rate of $2 \text{ m}^3\text{s}^{-1}$, both the
541 exfiltration surfaces and exfiltration rates are much higher in the restored situation. In other
542 words, the base flow regime of the restored situation is sufficient to positively impact the
543 interactions between surface and subsurface compartments of the Island. When forced
544 injections enhance the development of wetlands and maintain high rates of exfiltration over
545 long periods, from the mere hydrological standpoint, restoration works are successful.

546

547 *3.4. Suggestions for management practices*

548 The injection scenarios tested in the hydrological model with maximum peaks
549 reaching $80 \text{ m}^3\text{s}^{-1}$ are designed as a routine inlet for feeding Rohrschollen Island with water,
550 but some other inlet procedures can also be considered to improve the functioning of the
551 Island. We analyzed with the hydrological model how these routine injections could be
552 designed to maximize either the spatial extension of exfiltration areas maintaining wetlands in
553 surface or the time over which exfiltration occurs. Two hypothetical injections superimposed
554 to a base flow of $2 \text{ m}^3\text{s}^{-1}$ in the new channel were proposed, the first one being of short
555 duration (24 h) with an injection rate of $15 \text{ m}^3\text{s}^{-1}$, the second one being of longer duration
556 (120 h) but with a weaker injection rate of $5 \text{ m}^3\text{s}^{-1}$ (see Fig.12, up). As the total injected water
557 volume differs between both scenarios (the weaker injection flushes almost twice the volume
558 of the stronger injection), it can also be determined which of the two configurations—high
559 rate/small volume or small rate/high volume—maximizes extension and/or duration of
560 exfiltration.

561 Fig. 12 (down) plots the excess or lack of exfiltration surface areas during injections
562 compared with surface areas sustained by base flow ($2\text{m}^3\text{s}^{-1}$) in the new channel. The
563 evolution over time of these excess exfiltration areas (or lack thereof) occurs for both
564 injection scenarios with a lack of exfiltration areas occurring during the injection periods
565 when infiltration from the surface dominates. After the injection peak is completed, the
566 recession period—starting at $t = 52 \text{ h}$ for the high injection rate and $t = 162 \text{ h}$ for the small
567 injection rate (Fig. 12)—always shows an excess of exfiltration areas. The interesting point is
568 that the high injection rate delivers a smaller volume of water in the system but maintains
569 increased areas of exfiltration over extensive periods. For its part, the small injection rate has
570 no effect beyond $t = 250 \text{ h}$ with a system coming back to its initial state with $2\text{m}^3\text{s}^{-1}$ of routine

571 injection at the inlet. Finally, injecting less volume but with high injection rates over short
572 periods is better suited to maintaining exfiltration over long periods as the process feeding
573 wetlands on the Island (Fig. 12). It is also likely (though not studied in this work) that intense
574 injections favor the unclogging of the BGW, which are the primary surface water routes
575 contributing to water renewal on the Island.

576 **As already mentioned**, the short-term behavior of the hydrosystem in response to flood
577 events motivated this study. In a context where long-term horizons of the restoration benefits
578 are the principal objective, performing short-term simulations does not depart from this
579 prescribed objective. **The exploration of injection scenarios** discussed above with a model
580 highly resolved in time and space deciphers how the system currently behaves. Duplicating
581 that kind of simulations, **could for example inform** on the number and intensity of flood
582 events needed to maintain a prescribed number of exfiltration days (and mean flow rates) in a
583 year. In that sense, modeling short-term events is not necessarily in complete opposition with
584 long-term considerations on the modeled system.

585

586 **4. Conclusions**

587 Restoration projects to counterbalance the undesired effects of anthropogenic actions
588 on the hydrological, geomorphological, and ecological status of riverine ecosystems have
589 recently spread worldwide. As the interactions between surface and subsurface compartments
590 of the hydrosystem have a strong impact on hydrological, biogeochemical, and ecological
591 processes, it makes sense to rely upon integrated hydrological modeling when addressing the
592 question of restoration efficiency. When feasible (i.e., with tractable problems and models),
593 hydrological modeling with high resolution in time and space can accurately delineate
594 infiltration-exfiltration areas and their evolution over time as key factors for maintaining
595 active surface river networks

596 Relying upon simplified models, not in their physics but rather on their dimensionality
597 (as done in the present study), renders many problems tractable and calculable. This is the
598 case with Rohrschollen Island, which shows smooth variations of topography that do not help
599 to locate ground water outcrops. This comment also extends to the very transient hydraulic
600 behaviors requiring refined time steps to accurately capture temporal evolutions of the
601 system.

602 If the focus is placed on infiltration-exfiltration patterns as a reliable indicator of the
603 effects of restoration in riverine systems, any spatially distributed modeling exercise needs
604 conditioning regarding both model inputs and outputs. Concerning the conditioning (or
605 control) of model outputs associated with the delineation of exfiltration areas, the recent
606 technique of airborne, low altitude, and high-resolution thermal infrared imaging is very
607 promising. The technique is not free of measurement errors and artifacts, but it has been
608 shown reliable enough to highlight interactions between surface and subsurface compartments
609 of the hydrosystem that coincide with simulations. Further investigations should duplicate
610 thermal imaging over time with the aim of grasping the transient behavior of surface-
611 subsurface interactions and discussing the best versus the worst environmental conditions
612 where imaging is applicable.

613 Rohrschollen Island (and many other fluvial hydrosystems) is very specific regarding
614 surface-subsurface interactions, meaning that water heads in the aquifer are often close to
615 surface water levels. This means that slight variations in both compartments may invert the
616 direction of exchanged fluxes between compartments. In that case, injecting significant
617 volumes of water in a system to store them over large periods may be counterproductive, even
618 though these volumes may contribute to flooding over large areas. Large volumes are diverted
619 into the rapidly flowing surface water and exit the system. Intense injections of smaller
620 volumes over short periods foster intense local infiltration into the subsurface. The subsequent

621 water mounding in the aquifer then results in long-term storage and smooth release of water
622 via exfiltration. This behavior, hardly foreseeable, was that simulated for Rohrschollen Island
623 and could also apply to many other configurations of fluvial corridors. These results show that
624 management rules for a restored system may be developed from modeling exercises handling
625 various forcing scenarios applied to the system. If it is accepted that exfiltration (sustaining
626 ponding and wetlands) is a valuable indicator of riverine restoration, additional works should
627 envision various settings to improve this process. For example, it is not clear if several
628 smaller inlets could replace a single inlet in the system for higher efficiency. Is water
629 extraction from the surface and reinjection in the subsurface a valuable process that can
630 generate slow exfiltration over broad areas? Physically-based integrated modeling of
631 hydrosystems might propose some answers.

632

633 **Acknowledgements**

634 The monitoring of the Rohrschollen Island was funded by the European Community (LIFE08
635 NAT/F/00471), the City of Strasbourg, the University of Strasbourg (IDEX-CNRS 2014
636 MODELROH project), the French National Center for Scientific Research (CNRS), the
637 ZAEU (Zone Atelier Environnementale Urbaine - LTER), the Water Rhin-Meuse Agency, the
638 DREAL Alsace, the “Région Alsace,” the “Département du Bas-Rhin,” and the company
639 “Électricité de France.” The authors are also indebted to Pascal Finaud-Guyot for his
640 contribution in the preprocessing of hydrological datasets.

641

642 **References**

- 643 Ala-aho, P., Rossi, P. M., Isokangas, E., and Klove B.: Fully integrated surface subsurface
644 flow modelling of groundwater–lake interaction in an esker aquifer: Model verification with
645 stable isotopes and airborne thermal imaging, *J. Hydrol.*, 522, 391–406,
646 doi:10.1016/j.jhydrol.2014.12.054, 2015.
- 647 Boano, F., Harvey, J.W., Marion, A., Packman, A.I., Revelli, R., Ridolfi, L., and Wörman, A.:
648 Hyporheic flow and transport processes: Mechanisms, models, and biogeochemical
649 implications, *Rev. Geophys.*, 52, 603–679, doi:10.1002/2012RG000417, 2014.
- 650 Boulton, A.J., Datry, T., Kasahara, T., Mutz, M., and Stanford, J.A.: Ecology and
651 management of the hyporheic zone: stream–groundwater interactions of running waters and
652 their floodplains. *J. N. Am. Benthol. Soc.* 29 (1), 26–40, 2010.
- 653 Brunner, P., Therrien, R., Renard, P., Simmons, C.T., and Franssen, H.-J. H.: Advances in
654 understanding river-groundwater interactions, *Rev. Geophys.*, 55,
655 doi:10.1002/2017RG000556, 2017.
- 656 Camporese, M., Penna, D., Borga, M., and Paniconi C.: A field and modeling
657 study of nonlinear storage - discharge dynamics for an Alpine headwater catchment,
658 *Water Resour. Res.*, 50, doi: 10.1002/2013WR013604, 2014.
659
- 660 Clilverd, H.M., Thompson, J.R., Heppell, C.M., Sayer, C.D., and Axmacher, J.C.: Coupled
661 hydrological/hydraulic modelling of river restoration impacts and floodplain hydrodynamics.
662 *River Res. Appl.* 32, 1927–1948, 2016.
663
- 664 Danczak, R.E., Sawyer, A.H., Williams, K.H., Stegen, J.C., Hobson, C., and Wilkins, M.J.:
665 Seasonal hyporheic dynamics control coupled microbiology and geochemistry in Colorado
666 River sediments, *J. Geophys. Res. Biogeosci.*, 121, 2976–2987, doi:10.1002/2016JG003527,
667 2016.
668
- 669 Daniluk, T.L., Lautz, L.K., Gordon, R.P., and Endreny, T.A.: Surface water– groundwater
670 interaction at restored streams and associated reference reaches. *Hydrol. Process.* 27 (25),
671 3730–3746, 2013.
672
- 673 Eschbach, D., Piasny, G., Schmitt, L., Pfister, L., Grussenmeyer, P., Koehl, M., Skupinski, G.,
674 and Serradj, A.: Thermal-infrared remote sensing of surface water – groundwater exchanges
675 in a restored anastomosing channel (Upper Rhine River, France). *Hydrol. Process.* 31, 1113-
676 1124, 2017.
677
- 678 Eschbach, D., Schmitt, L., Imfeld, G., Preusser, F., Payraudeau, S., May, J.-H., Trauerstein,
679 M., and Skupinski, G.: Long-term trajectories of rivers to perform functional restorations: an
680 interdisciplinary case study on the Rhine River (Rohrschollen Island, France). *Hydrology and*
681 *Earth System Sciences*, 2717–2737, 2018.
682
- 683 Fatichi, S., Vivoni, E.R., Ogden, F.L., Ivanov, V.Y., Mirus, B., Gochis, D., Downer, C.W.,
684 Camporese, M., Davison, J.H., Ebel, B., Jones, N., Kim, J., Mascaro, G., Niswonger, R.,
685 Restrepo, P., Rigon, R., Shen, C., Sulis, M., and Tarboton, D.: An overview of current

686 applications, challenges, and future trends in distributed process-based models in hydrology.
687 J. Hydrol. 537, 45-60, 2016.
688

689 Friberg, N., Harrison, L., O'Hare, M., and Tullos, D.: Restoring rivers and floodplains:
690 Hydrology and sediments as drivers of Change, *Ecohydrology*, 10(5),
691 doi.org/10.1002/eco.1884, 2017.
692

693 Glaser, B.; Klaus, J., Frei, S., Frentress, J., Pfister, L., and Hopp, L.: On the value of surface
694 saturated area dynamics mapped with thermal infrared imagery for modeling the hillslope-
695 riparian-stream continuum. *Water Resour. Res.*, 52, 8317-8342, 2016.
696

697 Hammersmark, C.T., Dobrowski, S.Z., Rains, M.C. and Mount, J.F., 2010. Simulated effects
698 of Stream restoration on the distribution of Wet-Meadow vegetation. *Restor. Ecology*, 18(6),
699 882-893.
700

701 Hare, D.K., Briggs, M.A., Rosenberry, D.O., Boutt, D.F., and Lane, J.W.: A comparison of
702 thermal infrared to fiber-optic distributed temperature sensing for evaluation of groundwater
703 discharge to surface water. *J. Hydrol.* 530, 153–166, 2015.
704

705 Hazenberg, P., Fang, Y., Broxton, P., Gochis, D, Niu, G-Y., Pelletier, J.D., Troch, P.A., and
706 Zeng, X.: A hybrid-3D hillslope hydrological model for use in Earth system models. *Water*
707 *Resour. Res.* 10, 8218-8239, 2015.
708

709 Hazenberg, P., Broxton, P., Gochis, D., Niu, G-Y., Pangle, L.A., Pelletier, J.D., Troch, P.A.,
710 and Zeng, X.: Testing the hybrid-3-D hillslope hydrological model in a controlled
711 environment. *Water Resour. Res.* 52, 1089-1107, 2016.
712

713 Hester, E.T., Cardenas, M.B. Haggerty, R., and Apte, S.V.: The importance and challenge of
714 hyporheic mixing, *Water Resour. Res.*, 53, 3565–3575, doi:10.1002/2016WR020005, 2017.

715 Jeannot, B., Weill, S., Eschbach, D., Schmitt, L. and Delay, F.: A low-dimensional integrated
716 subsurface hydrological model coupled with 2-D overland flow: Application to a restored
717 fluvial hydrosystem (Upper Rhine River – France). *J. Hydrol.*, 563, 495-509, 2018.
718

719 Krause, S., Boano, F., Cuthbert, M.O., Fleckenstein, J.H., and Lewandowski, J.:
720 Understanding process dynamics at aquifer-surface water interfaces: An introduction to the
721 special section on new modeling approaches and novel experimental technologies, *Water*
722 *Resour. Res.*, 50, 1847–1855, doi:10.1002/2013WR014755, 2014.
723

724 Kurylyk, B.L., MacQuarrie, K.T.B., Linnansaari, T., Cunjak, R.A., and Curry R.A.:
725 Preserving, augmenting, and creating cold-water thermal refugia in rivers: concepts derived
726 from research on the Miramichi River, New Brunswick (Canada). *Ecohydrol.*, 8, 1095-1108,
727 2015.
728

729 Martinez-Martinez, E., Nejadhashemi, A.P., Woznicki, S.A., and Love, B.J.: Modeling
730 the hydrological significance of wetland restoration scenarios. *J. Environ.*
731 *Manage.* 133, 121–134, 2014.
732

733 Maxwell, R.M., Putti, M., Meyerhoff, S., Delfs, J-O., Ferguson, I.M., Ivanov, V., Kim, J.,
734 Kolditz, O., Kollet, S.J., Kumar, M., Lopez, S., Niu, J., Paniconi, C., Park, Y-J., Phanikumar,
735 M.S., Shen, C., Sudicky, E.A., and Sulis, M.: Surface–subsurface model inter-comparison: a

736 first set of benchmark results to diagnose integrated hydrology and feedbacks. *Water Resour.*
737 *Res.* 50, 1531-1549, 2014.

738

739 Morandi, B., Piegay, H., Lamouroux, N., and Vaudor, L.: How is success or failure in river
740 restoration projects evaluated? Feedback from French restoration projects. *J. Environ. Manag.*
741 137, 178-188, 2014.

742

743 Munz, M., Oswald, S., and Schmidt, C.: Coupled Long-Term Simulation of Reach-Scale
744 Water and Heat Fluxes Across the River-Groundwater Interface for Retrieving Hyporheic
745 Residence Times and Temperature Dynamics. *Water Resour. Res.*, 53, 8900-8924, 2017.

746

747 Namour, P., Schmitt, L., Eschbach, D., Moulin, B., Fantino, G., Bordes, C., and Breil, P.:
748 Stream pollution concentration in riffle geomorphic units (Yzeron basin, France). *Sci. Total*
749 *Environ.*, 532, 80–90, 2015.

750

751 Ohara, N., Kavvas, M. L., Chen, Z. Q., Liang, L., Anderson, M., Wilcox J., and Mink, L.:
752 Modelling atmospheric and hydrologic processes for assessment of meadow restoration
753 impact on flow and sediment in a sparsely gauged California watershed. *Hydrol. Process.*, 28,
754 3053-3066, 2014.

755

756 Pan, Y., Weill, S., Ackerer, P., and Delay F.: A coupled streamflow and depth-integrated
757 subsurface flow model for catchment hydrology. *J. Hydrol.* 530, 66-78, 2015.

758

759 Paniconi, C. and Putti, M.: Physically based modeling in catchment hydrology at 50: survey
760 and outlook. *Water Resour. Res.* 51, 7090-7129. <http://dx.doi.org/10.1002/2015WR017780>,
761 2015.

762

763 Partington, D., Brunner, P., Frei, S., Simmons, C.T., Werner, A.D., Therrien, R., Maier, H.R.,
764 Dandy, G.C., and Fleckensetein, J.H.: Interpreting streamflow generation mechanisms from
765 integrated surface-subsurface flow models of a riparian wetland and catchment. *Water*
766 *Resour. Res.* 9, 5501-5519. <http://dx.doi.org/10.1002/wrcr.20405>, 2013.

767

768 Partington, D., Therrien, R., Simmons, C. T., and Brunner, P.: Blueprint for a coupled model
769 of sedimentology, hydrology, and hydrogeology in streambeds, *Rev. Geophys.*, 55, 287–309,
770 doi:10.1002/2016RG000530, 2017.

771

772 Peralta-Maraver, I., Reiss, J., and Robertson, A.L.: Interplay of hydrology, community
773 ecology and pollutant attenuation in the hyporheic zone. *Sci. Total Environ.* 610,
774 267–275, 2018.

775

776 Pfister, L., McDonnell, J.J., Hissler, C., and Hoffmann, L.: Ground-based thermal imagery as
777 a simple, practical tool for mapping saturated area connectivity and dynamics, *Hydrol.*
Processes, 24(21), 3123–3132, doi:10.1002/hyp.7840, 2010.

778

779 Schmitt, L., Lafont, M., Trémolières, M., Jezequel, C., Vivier, A., Breil, P., Namour, P.,
780 Valin, K., and Valette, L. : Using hydro-geomorphological typologies in functional ecology:
781 Preliminary results in contrasted hydrosystems. *Phys. Chem. of Earth*, 36, 539–548, 2011.

782

781 Sophocleous, M.A.: Interactions between groundwater and surface water: the state of the
782 science. *Hydrogeol. J.* 10, 52–67, 2002.

783 Stegen, J.C., Fredrickson, J.K., Wilkins, M.J., Konopka, A.E., Nelson, W.C., Arntzen, E.V.,
784 Chrisler, W.B., Chu, R.K., Danczak, R.E., Fansler, S.J., Kennedy, D.W., Resch, C.T., and
785 Tfaily, M.: Groundwater–surface water mixing shifts ecological assembly processes
786 and stimulates organic carbon turnover. *Nat. Commun.* 7, 11237, 2016.
787
788 Stegen, J.C., James, C., Johnson, T., Fredrickson, J.K et al.: Influences of organic carbon
789 speciation on hyporheic corridor biogeochemistry and microbial ecology. *Nat. Commun.* 9,
790 1034, 2018.
791
792 Weill, S., Delay, F., Pan, Y., and Ackerer, P.: A low-dimensional subsurface model for
793 saturated and unsaturated flow processes: ability to address heterogeneity. *Computat. Geosci.*
794 21, 301-314, 2017.
795
796 Winter, T.C., Harvey, J.W., Franke, O.L., and Alley, W.M.: Ground water and surface water:
797 a single resource. Circular 1139, US Geological Survey, Denver, CO, 1998.
798
799 Wohl, E., Lane, S. N., and Wilcox, A.C.: The science and practice of river restoration, *Water*
800 *Resour. Res.*, 51, 5974–5997, doi:10.1002/2014WR016874, 2015.
801

802 **Figure captions**

803

804 Fig. 1. (a) location of the studied area (France), (b) aerial view of Rohrschollen Island, and (c)
805 network of hydrologic response measurements (mainly hydraulic heads and water fluxes).

806

807 Fig. 2. Digital elevation model of Rohrschollen Island (left) and location of the main gravel
808 bars reconstructed from the geo-historical and sedimentological studies (right). The black and
809 white lines correspond to transects of hydrologic measurements (see Figure 1).

810

811 Fig. 3. Evolution over time of flow rates injected in the new artificial channel feeding
812 Rohrschollen Island during the period selected for calibrating the integrated hydrological
813 model (up), and the period chosen as a validation (forecasting) exercise (down).

814

815 Fig.4. Calibrated fields of saturated hydraulic conductivity in the subsurface compartment
816 (left) and exchange coefficient between surface and subsurface compartments (right).

817

818 Fig. 5. Comparison between simulated and measured hydraulic heads in the subsurface during
819 the calibration period. Left: evolution over time at the two transects, that is, the worst (up) and
820 best (down) transects regarding RMSE. Right: Local in space and time values of simulated
821 hydraulic heads as a function of observed ones. RMSE = root of mean square error, and KGE
822 = Kling-Gupta efficiency.

823

824 Fig. 6. Comparison between simulated and measured hydraulic heads in the subsurface during
825 the validation period. Left: evolution over time at the two transects, that is, the worst (up) and
826 best (down) transects regarding RMSE. Right: local in space and time values of simulated
827 hydraulic heads as a function of observed ones. RMSE = root of mean square error, and KGE
828 = Kling-Gupta efficiency.

829

830 Fig 7. Comparison between simulated exfiltration patterns and thermal anomalies identified
831 via thermal infrared imaging close to the junction between the new channel (southeast corner)
832 and the BGW (Bauerngrundwasser; center of Fig.). Red transects a and b are locations where
833 surface water and groundwater head are followed to exemplify surface-subsurface interactions
834 in Fig 9.

835

836 Fig. 8. Groundwater head, surface water thickness, and exfiltration rate over the whole of
837 Rohrschollen Island for three different periods (in hours after the beginning of injection) of
838 the calibration period. Notably, the last period is also the date of the airborne thermal infrared
839 imaging.

840

841 Fig. 9. Evolution of surface water elevation (blue), groundwater head (red), and exchange
842 fluxes (arrows) along transects a and b (located in Fig. 7) at two periods (hours after the
843 beginning of injection) of the calibration period. A thick grey line represents the topographic
844 profile. The grey scale indicates values of the saturated hydraulic conductivity at the interface
845 between surface and subsurface.

846

847 Fig. 10. Evolution of the infiltration and exfiltration volumetric fluxes during the first steps of
848 the calibration period (where evolutions are essential).

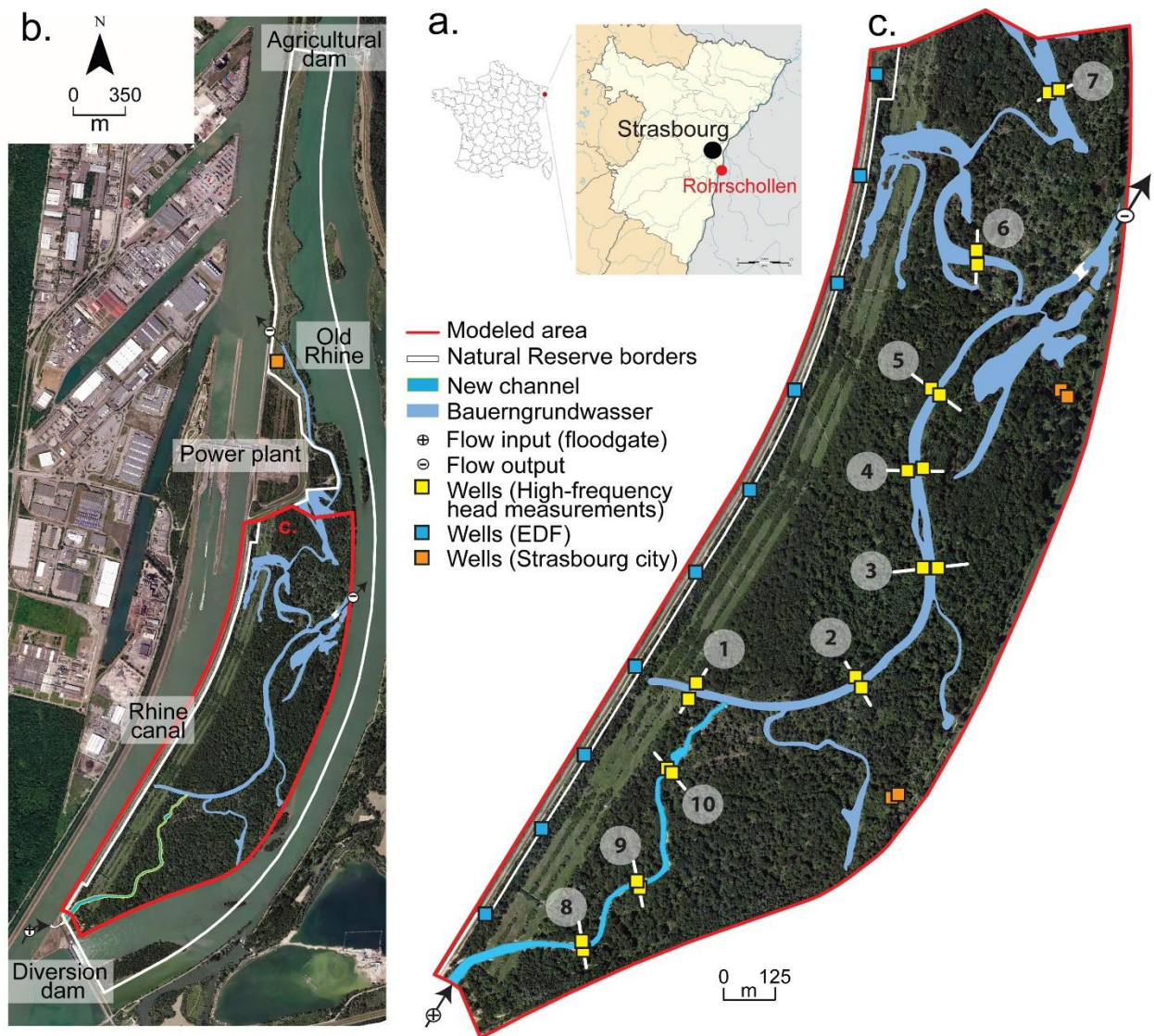
849

850 Fig. 11. Patterns of exfiltration for the pre-restored and the restored situations. The focus is on
851 the most active zone of Rohrschollen Island regarding surface-subsurface interactions.

852
853
854
855
856
857
858
859
860
861
862
863
864
865
866
867
868
869
870
871
872
873
874
875
876
877
878
879
880
881
882
883
884
885
886
887
888
889
890
891
892
893
894
895
896
897
898
899
900
901

Fig. 12. Up: injection rates of two scenarios seeking optimal exfiltration surface areas and durations at Rohrschollen Island. Down: Evolution over time of excess or lack of exfiltration surface area compared with exfiltration surface produced by a routine injection rate of $2 \text{ m}^3 \text{ s}^{-1}$ at the inlet of the system.

Table 1. List of parameters that were calibrated with initial and final value after calibration. Only the saturated hydraulic conductivity and the exchange coefficient were considered variable in space. The other parameters are considered homogeneous for the whole simulated domain.



902

903 **Fig 1.** (a) location of the studied area (France), (b) aerial view of Rohrschollen Island, and (c)
 904 network of hydrologic response measurements (mainly hydraulic heads and water fluxes).
 905

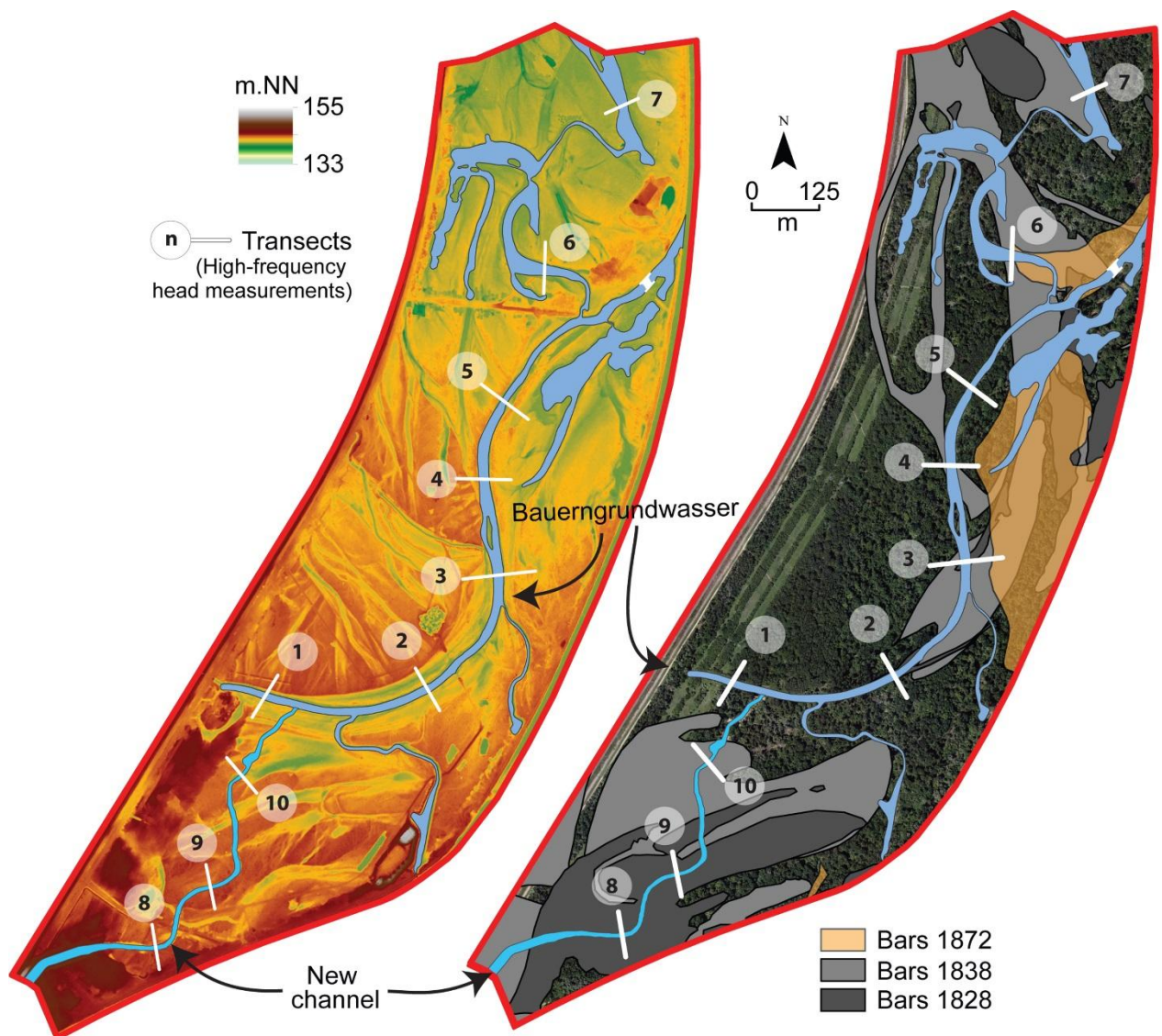
906

907

908

909

910



911

912

913 **Fig 2.** Digital elevation model of Rohrschollen Island (left) and location of the main gravel
 914 | bars reconstructed from the geo-historical and sedimentological studies (right). The black and
 915 | white lines correspond to transects of hydrologic measurements (see Figure 1).

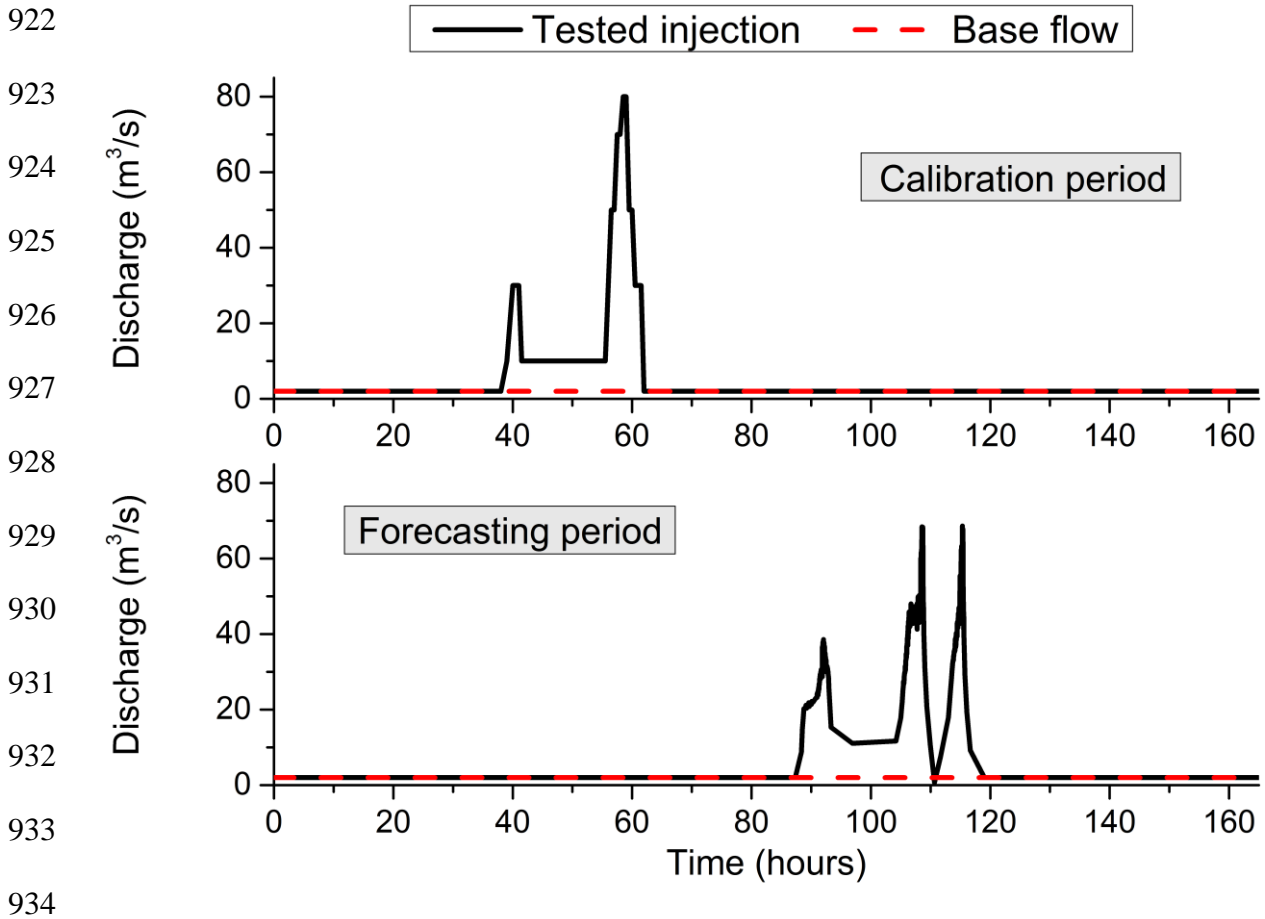
916
 917

918

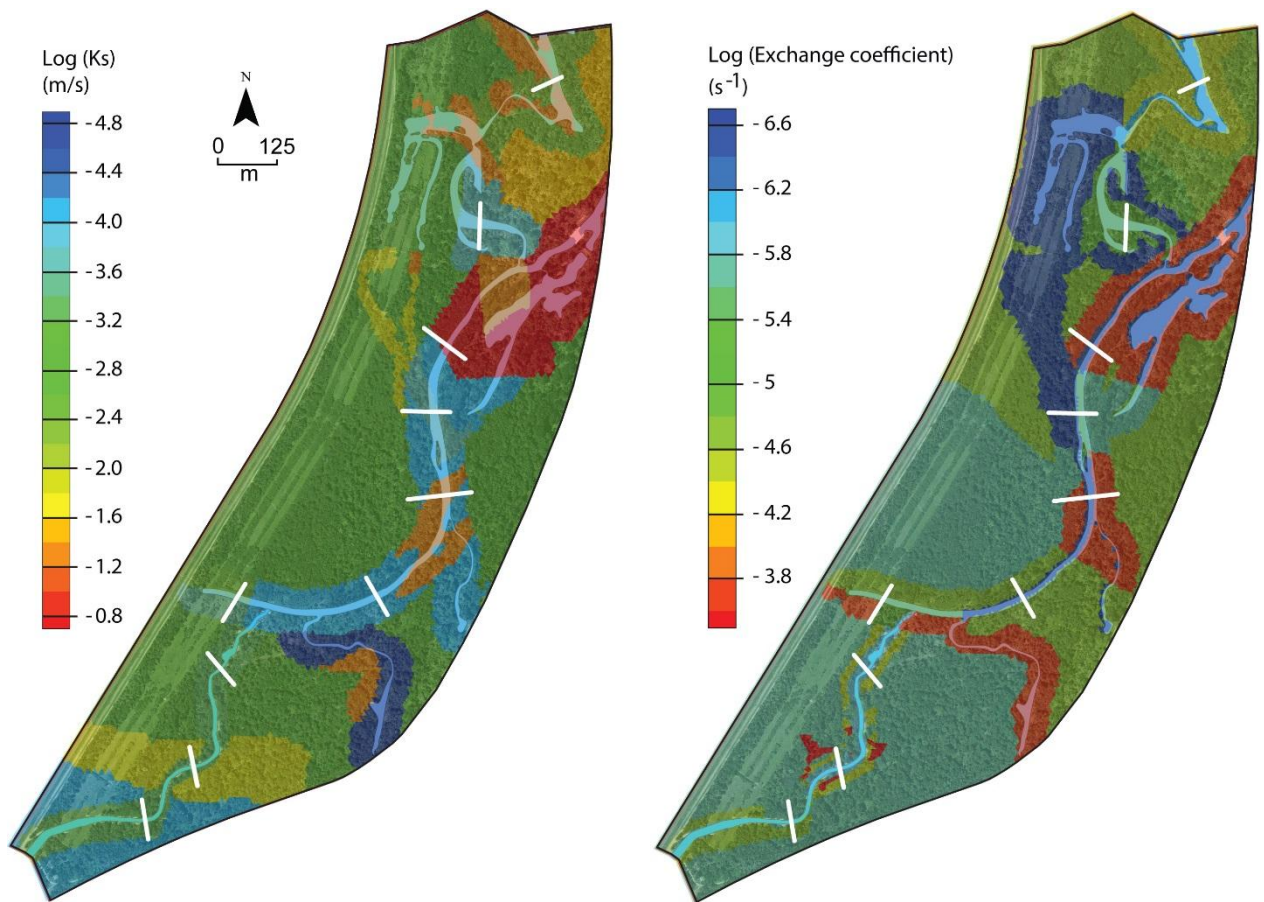
919

920

921



935 **Fig. 3.** Evolution over time of flow rates injected in the new artificial channel feeding
 936 Rohrschollen Island during the period selected for calibrating the integrated hydrological
 937 model (up), and the period chosen as a validation (forecasting) exercise (down). The red
 938 dashed line corresponds to the baseflow injection – i.e. an injected discharge of $2 \text{ m}^3 \text{ s}^{-1}$.



939

940

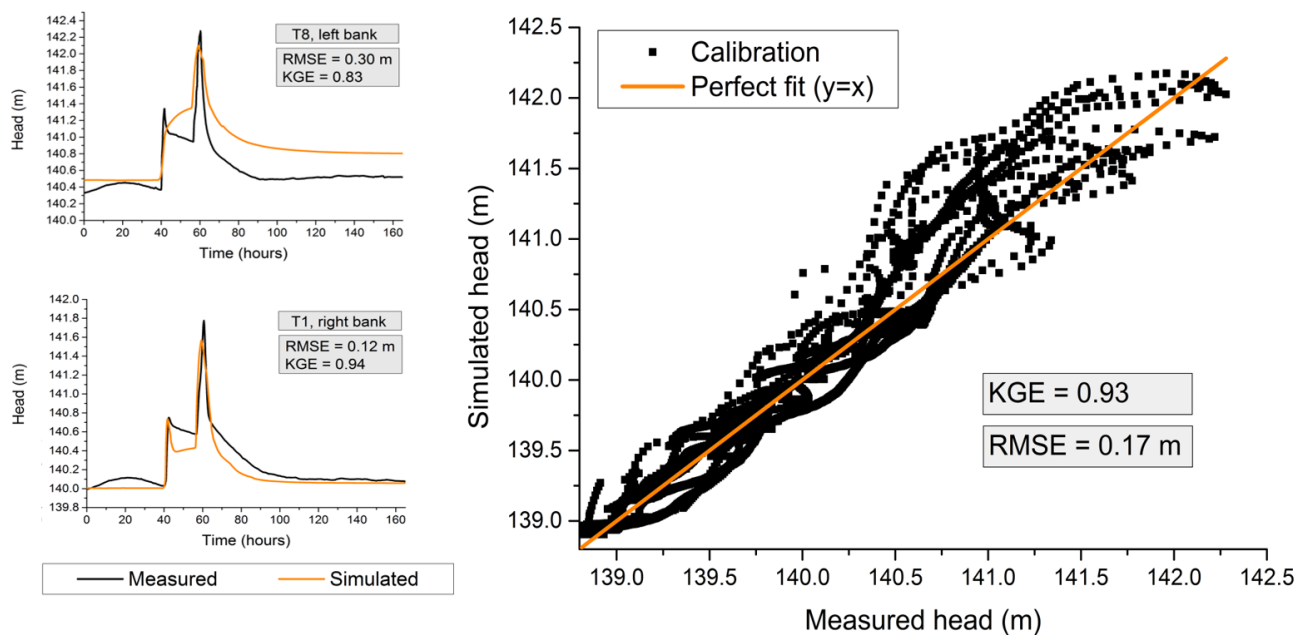
941 **Fig 4.** Calibrated fields of saturated hydraulic conductivity in the subsurface compartment
 942 (left) and exchange coefficient between surface and subsurface compartments (right).

943

944

945

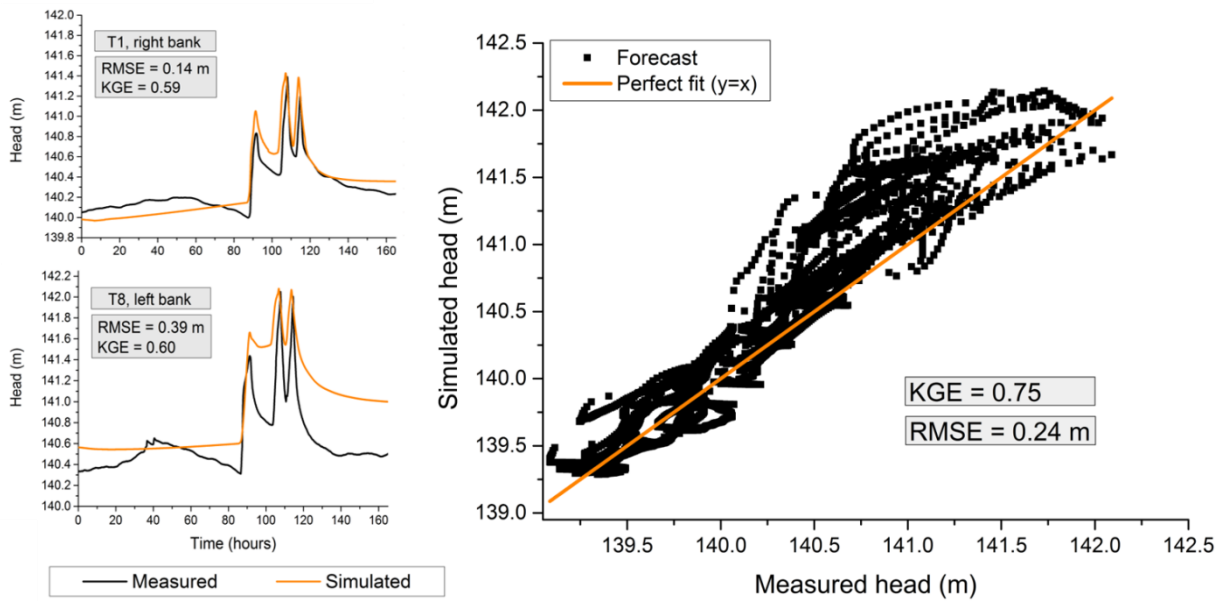
946



947

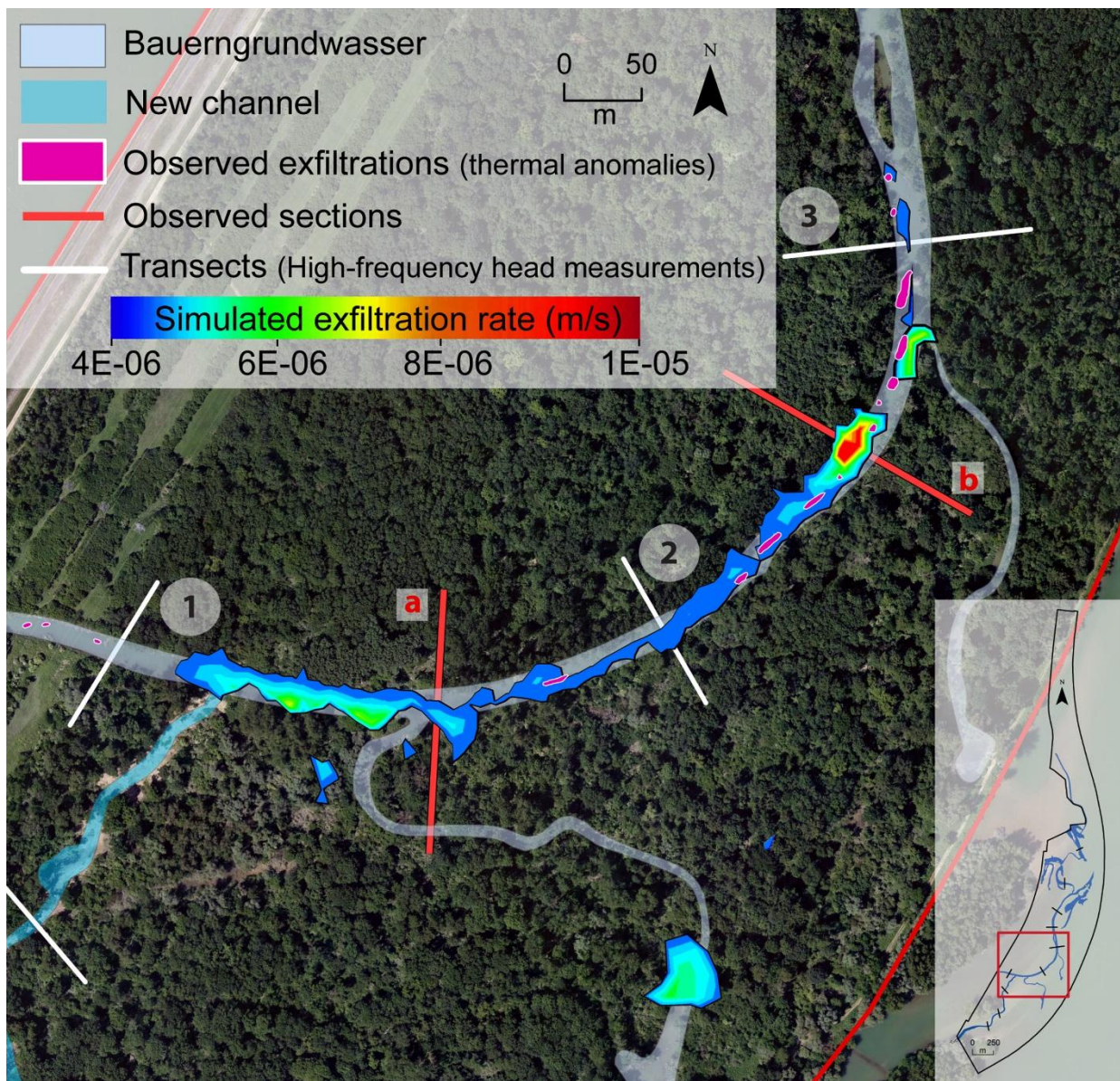
948 **Fig. 5.** Comparison between simulated and measured hydraulic heads in the subsurface during
 949 the calibration period. Left: evolution over time at the two transects, that is, the worst (up) and
 950 best (down) transects regarding RMSE. Right: Local in space and time values of simulated
 951 hydraulic heads as a function of observed ones. RMSE = root of mean square error, and KGE
 952 = Kling-Gupta efficiency. The KGE value for measured vs. simulated heads is associated with
 953 a Pearson correlation coefficient of 0.97, a bias ratio of 1, and a variance ratio of 1.07.

954
 955
 956
 957
 958
 959
 960
 961
 962
 963
 964
 965
 966
 967
 968
 969
 970
 971
 972
 973
 974
 975



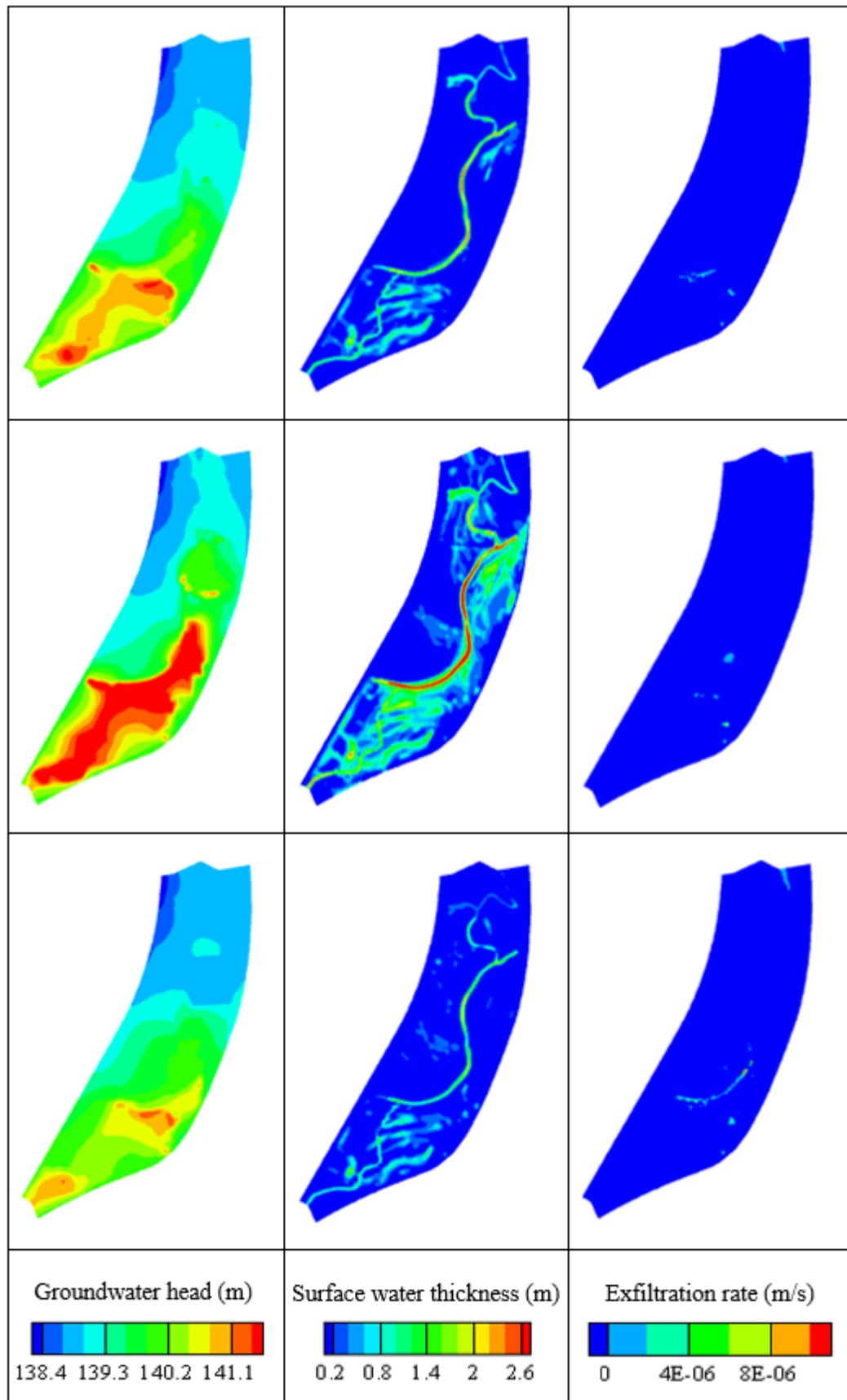
976
 977
 978
 979
 980
 981
 982
 983
 984

Fig. 6. Comparison between simulated and measured hydraulic heads in the subsurface during the validation period. Left: evolution over time at the two transects, that is, the worst (up) and best (down) transects regarding RMSE. Right: local in space and time values of simulated hydraulic heads as a function of observed ones. RMSE = root of mean square error, and KGE = Kling-Gupta efficiency. The KGE value for measured vs. simulated heads is associated with a Pearson correlation coefficient of 0.94, a bias ratio of 1, and a variance ratio of 1.24.



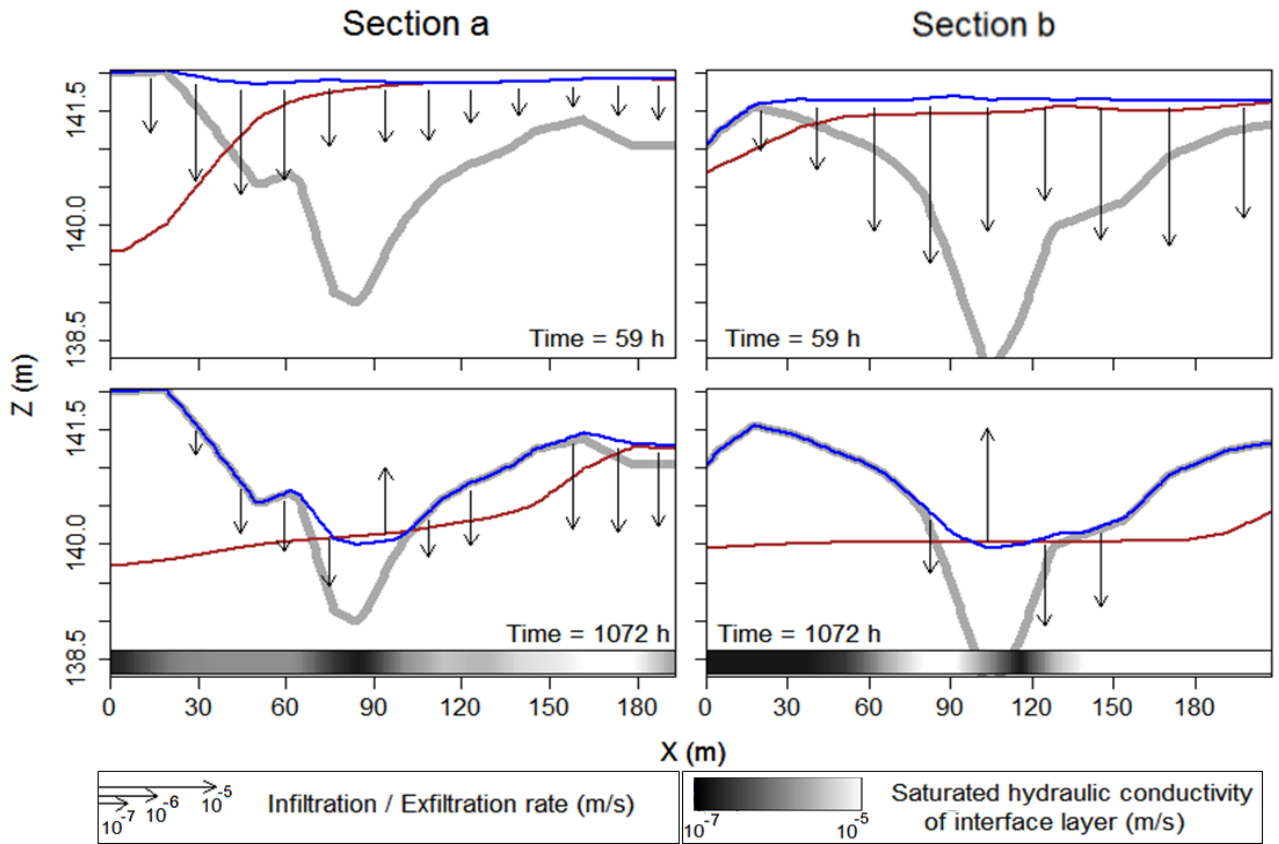
985

986 **Fig 7.** Comparison between simulated exfiltration patterns and thermal anomalies identified
 987 via thermal infrared imaging close to the junction between the new channel (southeast corner)
 988 and the BGW (Bauerngrundwasser; center of Fig.). Red transects a and b are locations where
 989 surface water and groundwater head are followed to exemplify surface-subsurface interactions
 990 in Fig 9.



991 **Fig 8.** Groundwater head, surface water thickness, and exfiltration rate over the whole of
 992 Rohrschollen Island for three different periods (in hours after the beginning of injection) of
 993 the calibration period. Notably, the last period is also the date of the airborne thermal infrared
 994 imaging.

995
996
997



998

999

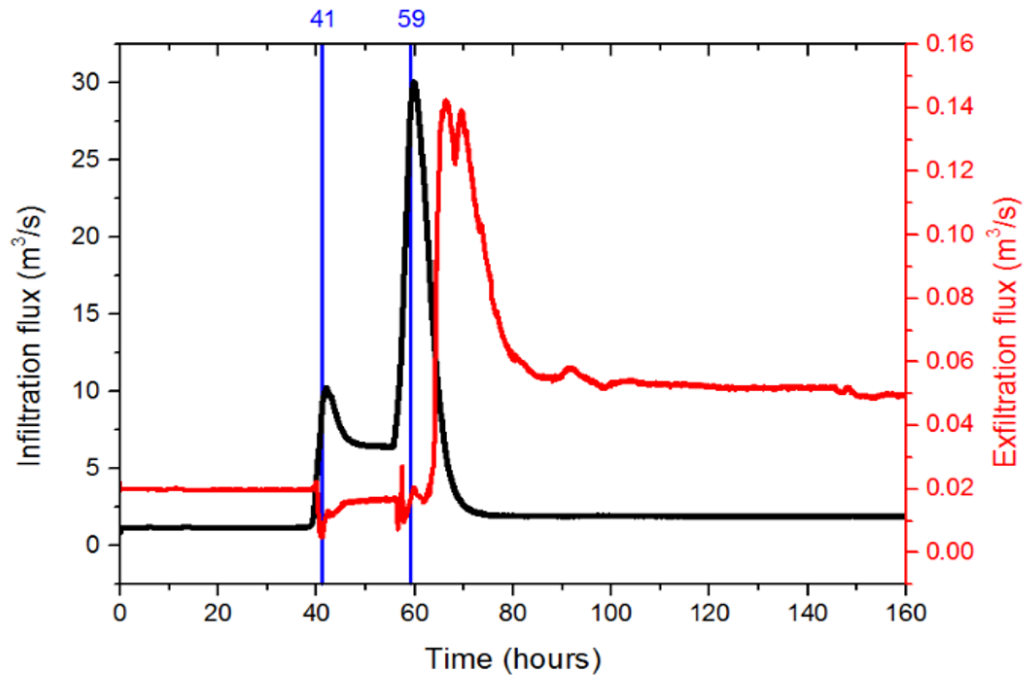
1000 **Fig. 9.** Evolution of surface water elevation (blue), groundwater head (red), and exchange
1001 fluxes (arrows) along transects a and b (located in Fig. 7) at two periods (hours after the
1002 beginning of injection) of the calibration period. A thick grey line represents the topographic
1003 profile. The grey scale indicates values of the saturated hydraulic conductivity at the interface
1004 between surface and subsurface.

1005

1006

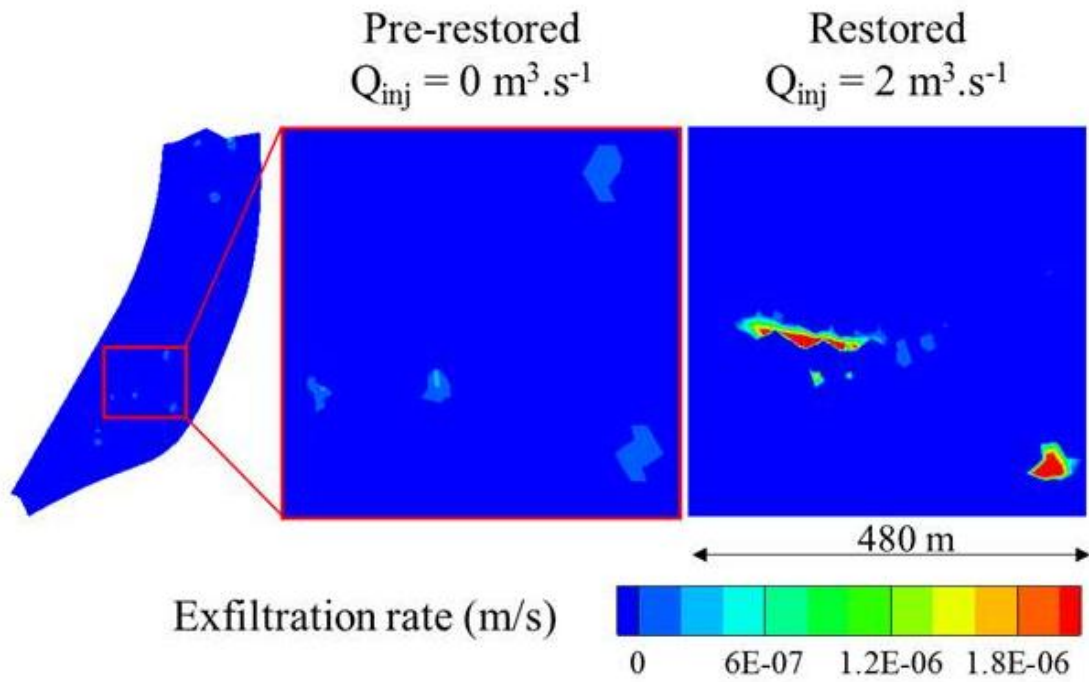
1007

1008



1009
 1010
 1011
 1012
 1013
 1014
 1015
 1016
 1017
 1018
 1019
 1020

Fig 10. Evolution of the infiltration and exfiltration volumetric fluxes during the first steps of the calibration period (where evolutions are essential).



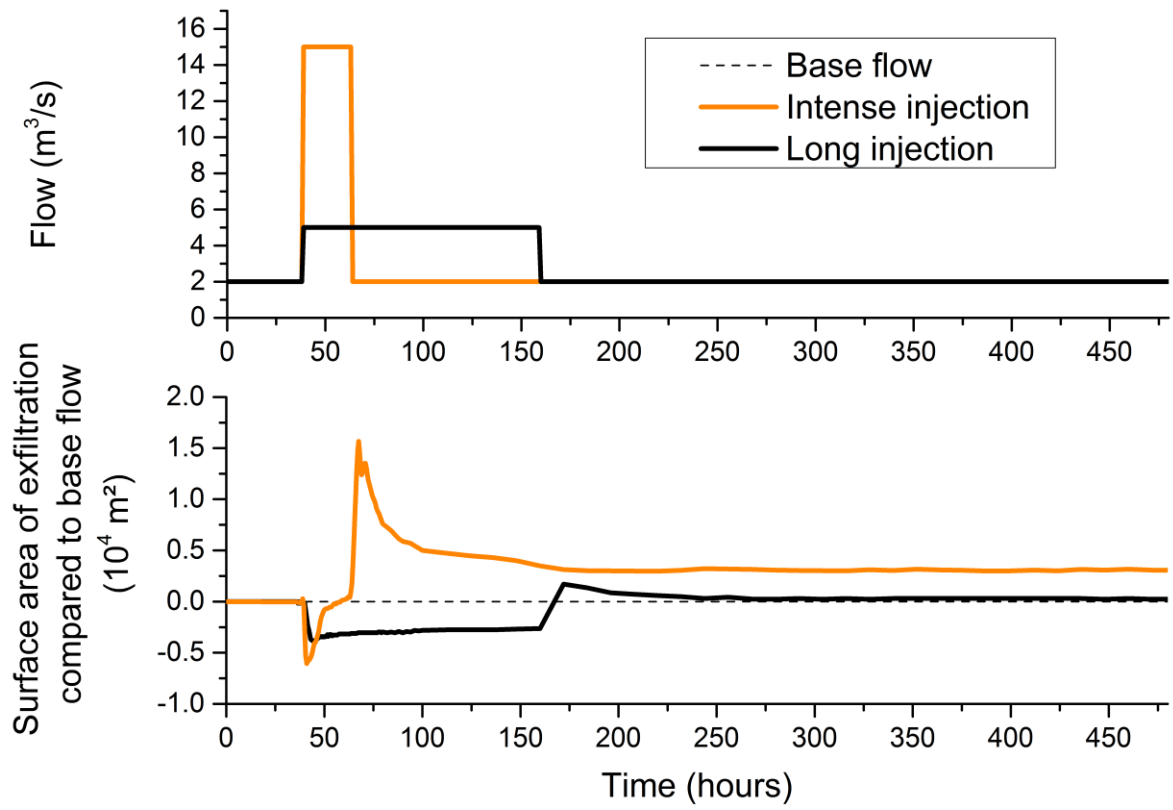
1021

1022 **Fig. 11.** Patterns of exfiltration for the pre-restored and the restored situations. The focus is on
 1023 the most active zone of Rohrschollen Island regarding surface-subsurface interactions.
 1024

1025

1026

1027



1029 **Fig 12.** Up: injection rates of two scenarios seeking optimal exfiltration surface areas and
 1030 durations at Rohrschollen Island. Down: Evolution over time of excess or lack of exfiltration
 1031 surface area compared with exfiltration surface produced by a routine injection rate of $2 \text{ m}^3 \text{ s}^{-1}$
 1032 at the inlet of the system.
 1033

1034

1035

1036

1037

1038

1039

1040

1041

1042

Parameters	Unit	Initial value	Calibrated value
Saturated hydraulic conductivity (averaged on the vertical)	m.s ⁻¹	1E-04	See Figure 4
Exchange coefficient (saturated hydraulic conductivity of the interface layer divided by the thickness of the interface layer)	m.s ⁻¹	1E-04	See Figure 4
Manning's coefficient	s.m ^{-1/3}	0.05	0.1
n (Van Genuchten coefficient) (first 50 centimeters)	-	2	1.53
n (Van Genuchten coefficient) (deeper than 50 centimeters)	-	2	3.18
α (Van Genuchten coefficient) (first 50 centimeters)	m ⁻¹	1	1.01
α (Van Genuchten coefficient) (deeper than 50 centimeters)	m ⁻¹	1	3.53
Porosity (first 50 centimeters)	-	0.4	0.41
Porosity (deeper than 50 centimeters)	-	0.4	0.38
Residual water content	-	0.08	0.05
Specific storage (first 50 centimeters)	m ⁻¹	1E-05	1E-04
Specific storage (deeper than 50 centimeters)	m ⁻¹	1E-05	1E-06

1043

1044

1045 **Table 1.** List of parameters that were calibrated with initial and final value after calibration.
1046 Only the saturated hydraulic conductivity and the exchange coefficient were considered
1047 variable in space. The other parameters are considered homogeneous for the whole simulated
1048 domain.

1049